Multiscale Molecular Thermodynamics of Graphene-oxide Liquid-phase Exfoliation

Journal:	*Physical Chemistry Chemical Physics*
Manuscript ID	CP-ART-11-2018-007115.R1
Article Type:	Paper
Date Submitted by the Author:	07-Dec-2018
Complete List of Authors:	Farajian, Amir; Wright State University, Mechanical and Materials Engineering Mortezaee, Reza; Wright State University, Mechanical and Materials Engineering Osborn, Tim; Wright State University, Mechanical and Materials Engineering Pupysheva, Olga; Wright State University, Mechanical and Materials Engineering Wang, Michael; Angstron Materials LLC Zhamu, Aruna; Angstron Materials, Inc., Jang, Bor; Angstron Materials, Inc.

SCHOLARONE™
Manuscripts

Multiscale Molecular Thermodynamics of Graphene-oxide Liquid-phase Exfoliation

Amir A. Farajian[1]*, Reza Mortezaee[1], Tim H. Osborn[1,†], Olga V. Pupysheva[1], Michael Wang[2], Aruna Zhamu[2], and Bor Z. Jang[2]

[1]*Department of Mechanical and Materials Engineering, Wright State University, 3640 Colonel Glenn Highway, Dayton, Ohio 45435, U.S.A.*

[2]*Angstron Materials LLC, 1240 McCook Avenue, Dayton, Ohio 45404, U.S.A.*

Abstract: Liquid-phase exfoliation is one of the most feasible methods for mass-production of two-dimensional (2D) nanomaterials such as graphene, graphene-oxide (GO), etc. Assessing requirements for successful exfoliation necessitates molecular-level thermodynamic analysis that can provide quantitative measures such as free energy changes. Here we explain this methodology and apply it to the production of GO that is used as a precursor for graphene synthesis and as an ultrathin substrate for many applications. Three different routes to GO exfoliation are studied, namely parallel and perpendicular to the GO surface as well as exfoliation via edge bending, using multi-scale combination of density functional, force field, and continuum approaches. Detailed analysis of free energy variations reveals relative feasibility of different exfoliation mechanisms and their dependence on system size and surface coverage. The methodology is general and can be applied to liquid-phase exfoliation of other 2D nanomaterials.

* Corresponding author: E-mail: amir.farajian@wright.edu

† Present address: Multiscale Composites and Polymers Division, University of Dayton Research Institute, Dayton, Ohio 45469, USA

TOC graphics:

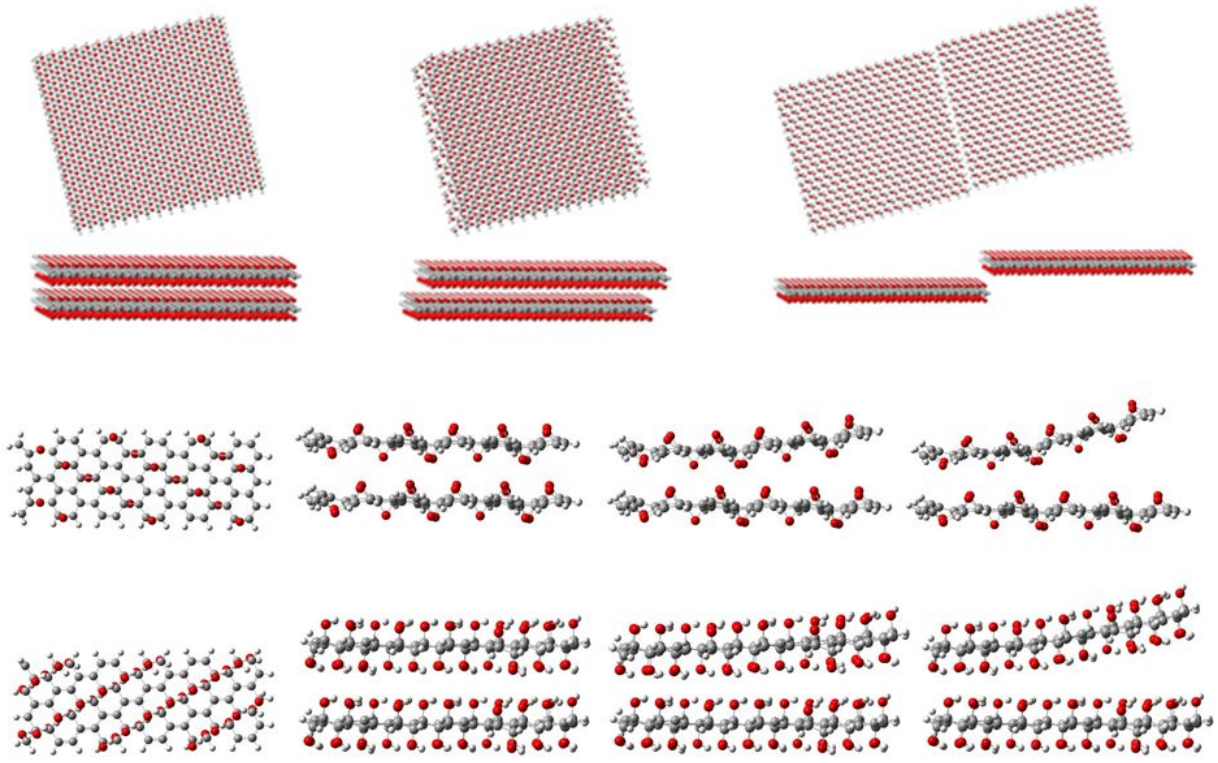

The general thermodynamic characteristics of 2D nanomaterials exfoliation are analyzed by considering different possible routes to graphene-oxide exfoliation as an example. Multi-scale thermodynamic modeling is used to quantitatively assess and compare free energy changes for various surface coverages and water adsorption possibilities. These reveal relative feasibility of different exfoliation mechanisms and their dependence on system characteristics.

1. Introduction

Large-scale exfoliation is one of the most efficient methods for mass production of 2D nanomaterials. This procedure has been used to produce defect- and oxide-free graphene sheets by exfoliation of graphite in organic solvents [1]. The method is direct, simple, benign, and as-obtained sheets are dispersed in liquid facilitating manipulation and subsequent processes [2]. In addition to graphene, individual carbon nanotubes in liquid phase have also been produced by exfoliation [3]. Furthermore, other 2D nanomaterials, e.g. nanoparticle-decorated graphene [4], molybdenum disulfide (MoS_2) [5], and phosphorus atomic layers [6], have been produced by liquid-phase exfoliation.

Graphene oxide (GO) is a 2D nanomaterial composed of single layer honeycomb sheet of carbon covered with oxygen-containing functional groups. Epoxy and hydroxyl groups are two main functional groups containing oxygen covering GO [7,8]. The stacked configuration, graphite oxide, has increased interlayer distance compared to graphite. One of the main applications of GO is in production of graphene through reduction. Wrinkled single sheets of functionalized graphene were obtained through thermal exfoliation of GO [9]. Reduction in the presence of hydrogen gas [10], Ar plasma treatment [11], vacuum-assisted thermal treatment [12], and focused solar radiation [13] resulted in production of graphene sheets from exfoliated GO. Thermal exfoliation of GO in hydrogen sulfide, sulfur dioxide, or carbon disulfide was shown to result in sulfur-doped graphene that was used as metal-free electrocatalyst [14]. Exfoliation and reduction of GO at various temperatures were recently investigated and smooth decrease of oxygen content, accompanied by restoration of pristine graphene, was observed upon increasing temperature [15].

In addition to graphene production, GO has been utilized in various other applications. Free standing GO paper, an assembly of individual GO sheets, was synthesized and shown to possess superior stiffness and strength [16]. Placing of single-layer GO on gold was achieved through amino-terminated templates, as, in contrast to carbon nanotubes, GO did not directly attach to the gold substrate [17]. GO has been used as transparent support for electron microscopy [18], in flexible organic photovoltaic cells [19], and for lithium storage [20]. It was also shown that GO has superior proton conductivity [21].

The importance of the aforementioned applications and the feasibility of GO production via exfoliation of graphite oxide necessitate in-depth analysis of this procedure. This will provide detailed information about factors relevant to exfoliation and its optimization. Some recent works report on the exfoliation process of GO: Graphite oxide treated with organic isocyanates resulted in exfoliated GO well dispersed in polar aprotic solvents [22]. Tetrabutylammonium cations [23], ferrocene [24], propylene carbonate [25], macromolecular polyaniline [26], and amphiphilic hyperbranched polymers [27] were used to exfoliate GO. Controlling the size of GO sheets was shown to be possible by choosing oxidation time and the amount of oxidants [28]. Magnetic stirring was also utilized in GO exfoliation [29]. Intercalation, grafting, and subsequent exfoliation of GO were carried out in styrene under γ-ray irradiation to produce functionalized graphene [30]. Platinum acetylacetonate and thermal treatment were also used to generate functionalized graphene from GO [31].

The present study focuses on multi-scale modeling of GO exfoliation thermodynamics. The presence of hydrophilic groups in GO is essential in the aforementioned applications and characteristics. In particular, GO exfoliation from graphite oxide in aqueous solution crucially depends on the density and arrangements of these groups. In a previous work [32] we explained a possible surfactant-based mechanism for direct exfoliation of graphene nanoplatelets [33]. The predicted vibration frequencies [32] were comparable to subsequently measured values [34]. Here, free energies for different GO exfoliation routes are calculated, and the role of water adsorption is explored in details, for various surface coverages. It is shown that the exfoliation proceeds step-by-step while adsorbed water molecules prevent restacking. Quantitative measures for assessing relative feasibility of different exfoliation mechanisms are provided, and their dependence on system characteristics is discussed.

2. Model and methods

The arrangement of epoxy and hydroxyl groups on the GO surface generally does not show long-range order. However, to estimate interactions between GO layers we initially consider periodic structures and use density functional theory (DFT) within local density approximation (LDA). LDA is shown to perform well for bilayer graphene-like systems, with predicted interlayer separation close to the experimental value [35,36]. Unit cells containing eight carbon atoms and various configurations and coverages of epoxy and hydroxyl groups are considered, and the corresponding periodic single-layer structures are optimized. The optimized single-layer structures are next stacked, considering various bilayer stacking arrangements in simulation unit cell, and are in turn optimized within LDA with periodicity imposed both parallel to the GO planes and

perpendicular to them. The DFT-LDA optimizations are performed using Ceperley-Alder (CA) pseudopotentials within SIESTA software [37,38], with all forces in relaxed structures less than 0.03 eV/Å. We use double-ζ basis with polarization (DZP), *k*-grid cutoff corresponding to 80 Bohr, and 3D mesh cutoff of 250 Ry. These settings were shown to satisfy standard convergence tests for graphene [39].

Using DFT-LDA structure optimization results, bilayer GO nanoplatelets in the form of squares with 40 Å side lengths are constructed, whose edges are saturated by hydrogen. These bilayer nanoplatelets are subsequently used to calculate effective force constants as well as changes in entropy, internal energy, and free energy. To account for the finite size of the nanoplatelets and the necessity to perform calculations including van der Waals interactions on systems with many atoms (on the order of few thousands), these calculations are carried out using the universal force field (UFF) approach [40] implemented in the Gaussian 09 program [41] while the interlayer distances are set at their UFF equilibrium values. For bilayer GO square nanpoplatelets that we simulate using UFF, no periodicity is imposed. We consider a geometric arrangement where Cartesian *x* and *y* axes are parallel to the edges of the square nanoplatelets, and *z* axis is perpendicular to them.

We analyze and compare three main possible exfoliation routes: (1) parallel and (2) perpendicular to GO surface without bending of the nanoplatelets, as well as (3) via bending at the edge. In the stacked state, the two GO sheets have basically similar *x* and *y* coordinates (with relative orientation determined by bilayer optimizations) but the 'top' layer is shifted along the *z* axis with

respect to the 'bottom" layer. At the verge of full parallel exfoliation, in addition to the *z* shift, the top layer is also shifted in plane (e.g., along *x* axis) by an amount equal to the square side length, i.e. 40 Å. For exfoliation perpendicular to the GO surface and via edge bending, the verge of full exfoliation is when the perpendicular distance between the two layers is increased so as to accommodate layers of solvent molecules whose interactions resemble those in solvent environment. The internal energy and entropy changes are calculated as the differences between corresponding quantities for the bilayer system in exfoliated and stacked states.

To assess GO cohesion strength for different surface groups and coverages, cohesive energies of single layer structures are compared using the following definition

$$E_{\text{cohesive}} = \frac{E_{\text{t,s}} - \sum_i N_i E_i}{\sum_i N_i}, \quad (1)$$

in which $E_{\text{t,s}}$, N_{i}, and E_{i} represent (per unit cell) single-layer total energy, number of atoms of *i* type, and energy of a single *i*-type atom not interacting with any other atom, respectively. It should be mentioned that the cohesive energy used here refers to single-layer structures only.

We estimate the strength of van der Waals interactions between the layers using

$$E_{\text{vdW}} = E_{\text{t,b}} - 2E_{\text{t,s}}, \quad (2)$$

where E_{vdW} and $E_{\text{t,b}}$ represent the interlayer van der Waals interaction and total energy of bilayer structure per unit cell, respectively.

For the process of bilayer GO exfoliation in aqueous solution at constant pressure and temperature, we can safely assume that the volume change ΔV is negligible as both GO and water are incompressible. Therefore, the enthalpy change $\Delta H = P\Delta V + \Delta U$ and the energy change ΔU are taken to be the same. The change in Gibb's free energy ΔG is thus given by:

$$\Delta G = \Delta H - T\Delta S \approx \Delta U - T\Delta S\,, \quad (3)$$

in which, T is absolute temperature, $\Delta U = \Delta U_K + \Delta U_{int}$ where ΔU_K is the change in kinetic energy arising from translational, rotational, and vibrational movements, ΔU_{int} is the change in internal (potential) energy, and ΔS is the entropy change upon exfoliation. ΔU_{int} is readily obtained by the UFF interlayer energy difference between the exfoliated and stacked states for the parallel and perpendicular exfoliations, and as the sum of inter- and intra-layer interactions for exfoliation via edge-bending. Treating the system under canonical ensemble conditions, ΔS, arising from motion of the two layers, is given by [42, 43]

$$\Delta S = S_{exf} - S_{sta} = k_{\mathrm{B}}\ln\left(\frac{q_{exf}}{q_{sta}}\right) + k_B T\left[\frac{\partial}{\partial T}\ln\left(\frac{q_{exf}}{q_{sta}}\right)\right]_{N,V}, \quad (4)$$

where subscripts *sta* and *exf* refer to stacked and exfoliated states, k_{B} is the Boltzmann constant, and q represents partition function. The second term on the right hand side of Eq. (4) is equal to $\Delta U_K/T$ [42, 43] and cancels the contribution of ΔU_K in ΔG.

Substituting the rotational and vibrational partition functions [44] corresponding to rotations around x, y, and z axes for bilayer and single layer structures (i.e., stacked and exfoliated

configurations, respectively) as well as interlayer vibrations of the layers in bilayer stacked state, we obtain

$$\ln\left(\frac{q_{exf}}{q_{sta}}\right) = \ln\left[\frac{\left(\theta_{\mathrm{rot}b,x}\,\theta_{\mathrm{rot}b,y}\,\theta_{\mathrm{rot}b,z}\,\pi\,T^3\right)^{\frac{1}{2}}}{\theta_{\mathrm{rots},x}\,\theta_{\mathrm{rots},y}\,\theta_{\mathrm{rots},z}}\right] + \sum_{i=1}^{6}\ln\left(\frac{1-e^{-h\nu_i/k_{\mathrm{B}}T}}{e^{-h\nu_i/2k_{\mathrm{B}}T}}\right). \quad (5)$$

Here, h is Planck's constant, $\theta_{\mathrm{rot}b,x}$ calculated as $\theta_{\mathrm{rot}b,x} = h^2/8\,\pi^2\,I_{b,x}\,k_{\mathrm{B}}$ is the characteristic temperature of rotation of the bilayer (stacked) configuration around x axis, and $I_{b,x}$ is the corresponding moment of inertia, $\theta_{\mathrm{rots},x}$ is the characteristic temperature of rotation of a single sheet (i.e. exfoliated configuration) around x axis. We have ignored the vibrations of atoms within each layer and consider only vibrations of two stacked layers relative to each other, as the in-layer vibrations are basically the same for the exfoliated and stacked states and their contribution to ΔG is therefore canceled. ν_i are the interlayer vibration frequencies for the stacked configuration corresponding to three modes of relative shifts of layers along x, y, and z axes, $\nu_i = (1/2\pi)\sqrt{k_{sh,i}/\mu}$, and three modes of relative tilts of layers around x, y, and z axes, $\nu_i = (1/2\pi)\sqrt{k_{t,i}/I_r}$, with corresponding effective force constants $k_{sh,i}$ (in units of J/m^2) for shifts and $k_{t,i}$ (in units of J/rad^2) for tilts, reduced mass μ, and reduced moment of inertia I_r, respectively. The effective force constants are calculated by parabolic fits to the UFF energy variation upon small shift/tilt values around minimum energy configurations of bilayer GO. For deriving Eq. (5) we have ignored the change in translational degrees of freedom and interlayer vibrations at the verge of exfoliation. Equation (5) is valid in the limit $T \gg \theta_{\mathrm{rot1},i}$, $\theta_{\mathrm{rot2},i}$ that is seen to be satisfied at T = 298 K.

The entropy of a free molecule generally decreases upon dissolving in a solvent. Different models have been used to estimate this effect, e.g., the models by Wertz [45] and Mammen et al. [46]. To estimate the entropy change in presence of solvent, here we use the Wertz model where ~50% of gas-phase entropy is lost upon dissolving in water [45,47,48]. As our UFF calculations do not include any water molecule, they correspond to "gas-phase" molecular simulations. In other words, the energetics of all systems involving GO square nanoplatelets (single layer, partially exfoliated bilayer, and fully stacked bilayer) are determined using UFF simulations without explicitly including water molecules. The dielectric effect of solvent environment, creation of two new solvent surfaces upon exfoliation, and adsorption of water molecules on the corresponding exposed areas are included in the free energy change. This is achieved by using a continuum approximation for the former two effects and ab initio calculations for the latter. Effect of solvent environment on ΔU_{int} can in principle be included via, e.g., calculating partial atomic point charges and using them to estimate electrostatic interactions within the polarizable continuum model in conjunction with UFF simulation. Owing to the large number of atoms considered in the present study, however, this approach is prohibitively demanding. Instead, we estimate the effect of solvent environment on ΔU_{int} by dividing ΔU_{int} by ε, the dielectric constant of water. This is based on the assumption that, upon exfoliation in aqueous medium, there are enough water molecules adjacent to the exposed surfaces to screen their interactions. These water molecules are at a distance of approximately 3 Å [49,50] from the bare graphene areas (not containing epoxy or hydroxyl groups) owing to the hydrophobic nature of bare graphene, and at a distance determined by hydrogen bond formation from the areas containing epoxy or hydroxyl groups. The changes in free energy is therefore given by

$$\Delta G = \frac{\Delta U_{int}}{\varepsilon} - 0.5 k_B T \ln\left(\frac{q_{exf}}{q_{sta}}\right) + 2\gamma\Delta A - 2\Delta E_{ads}, \quad (6)$$

where γ stands for surface energy density of the solvent, ΔA is the exposed surface area of each GO nanoplatelet, and ΔE_{ads} is the adsorption energy change arising from solvent molecules adsorption on the exposed surface of each GO nanoplatelet. Notice that all solvent effects are included in Eq. (6) through non-partition-function terms. The only effect of solvent on (gas phase) partition function term is to multiplpy it by 0.5, according to the model mentioned above. For the water solvent considered in the present work, the dielectric constant and surface energy density are 78.3 and $71.9 \times 10^{-3} Jm^{-2}$, respectively.

3. Results and discussion

3.1. Structure optimization and energetics

Both single-surfactant and mixed coverages of GO are considered for ab initio optimization. For coverage with one type of functional group, we consider four different GO bilayer configurations that are 100% covered and eight GO bilayer structures that are 50% covered including either epoxy or hydroxyl groups as initial configurations for DFT-LDA periodic optimization. Although the coverage in experimentally realized GO is usually less than these percentages, we choose these coverage ratios (together with the 75% mixed coverage to be explained shortly) to make the DFT-LDA calculations manageable, as they need relatively small supercells. However, the results allow some conclusions to be drawn about lower coverages as well. These initial structures are depicted in Fig. S1 of the Electronic Supplementary Information (ESI). Bilayer structure optimizations generally result in adjustment of interlayer spacing and rearrangement of relative orientations of

the GO layers. In case of large initial interlayer spacing, the interlayer interactions are negligible and no interlayer optimization occurs. In such cases, proper initial guesses are prepared for the DFT-LDA periodic calculations based on UFF energy estimates versus interlayer distance for 40 Å bilayer square sheets. After DFT-LDA periodic optimizations are accomplished, the minimum energy structures from each set with the same type of oxygen-containing group and surface coverage is selected. The resulting four minimum energy structures are depicted in Fig. 1. It is observed that in the optimized structures the bilayers are arranged so that the oxygen-containing surface groups from one layer tend to sit above/below regions of the neighboring layers that are not covered with surface groups.

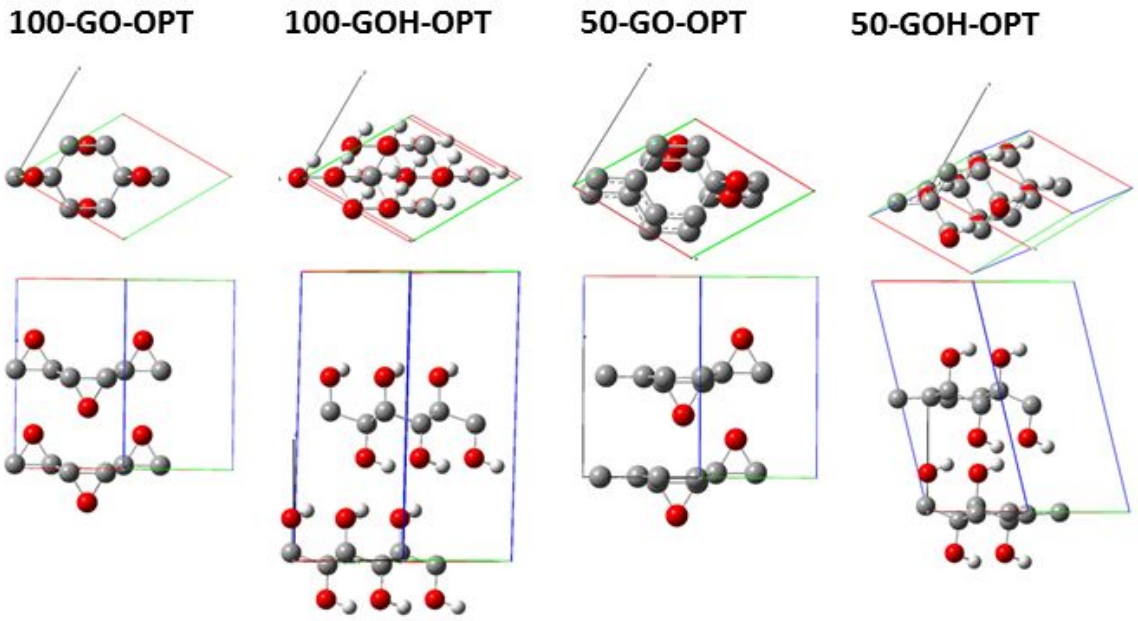

Figure 1: Top and side views (perpendicular and parallel to GO planes, respectively) of the unit cells of minimum energy configurations with 100 and 50% coverage of epoxy or hydroxyl group after DFT-LDA bilayer optimization. The optimized structures 100-GO-OPT, 100-GOH-OPT, 50-

GO-OPT, and 50-GOH-OPT result from relaxation of 100-GO-AA, 100-GOH-AB, 50-GO-AB-COIN, and 50-GOH-AA-NCOIN introduced in Fig. S1 of the ESI, respectively.

In addition to structures containing either epoxy or hydroxyl group, we also consider a hybrid structures with 75% coverage containing both of these groups. The hybrid arrangement is determined to be one of the possible realistic structures of GO [51]. Several initial bilayer structures with this hybrid arrangement are optimized and the minimum energy structure is obtained. In Fig. 2 we present the particular initial structure that resulted in the most stable optimization output, together with the optimized structure.

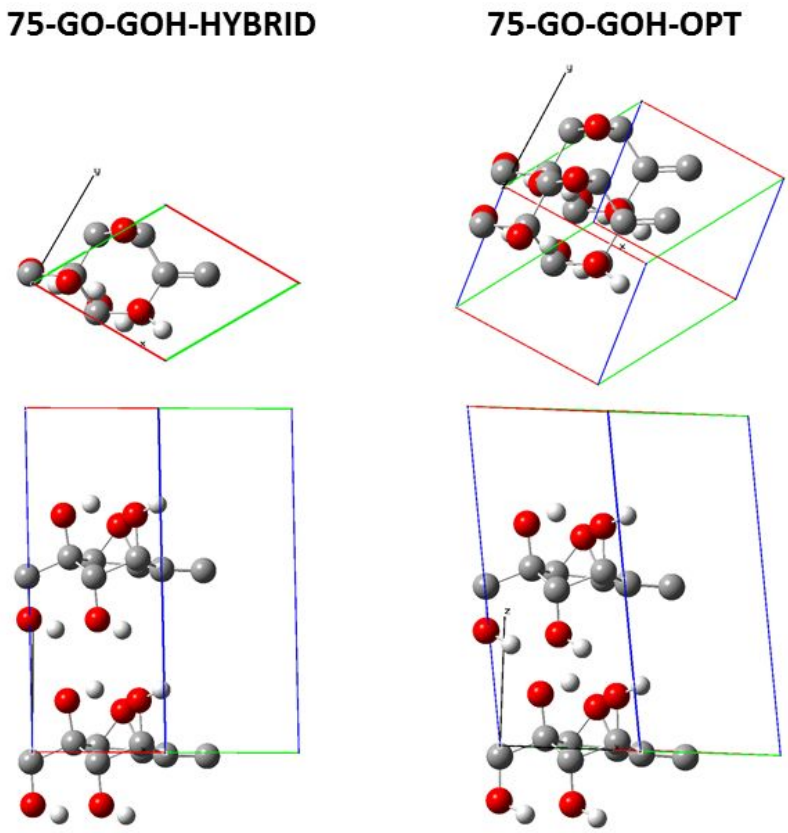

Figure 2: Top and side views of the initial (left) and final (right) hybrid structure that contains one epoxy and four hydroxyl groups per unit cell per layer, and results in minimum energy configuration after DFT-LDA optimization. The coverage in this 75-GO-GOH-HYBRID structure is 75%.

Table 1: Single-layer cohesive energy and van der Waals interlayer energy for the minimum-energy DFT-LDA optimized periodic structures, as well as average interlayer distance for the minimum-energy bilayer square platelets obtained from UFF calculations.

Structure	100-GO-OPT	100-GOH-OPT	50-GO-OPT	50-GOH-OPT	75-GO-GOH-OPT
Single layer cohesive energy (eV/atom)	-8.116	-6.558	-8.598	-7.261	-7.148
Interlayer van der Waals energy (eV/unit cell)	-3.772	-0.736	-2.487	-2.042	-2.085
Interlayer distance (Å)	4.45	6.27	4.30	5.33	5.79

In Table 1 we present the cohesive energy for a single GO layer and interlayer van der Waals energy for the optimized structures depicted in Figs. 1 and 2, as well as average interlayer distance for the minimum-energy bilayer square platelets obtained from UFF calculations. The single layer cohesive energy values in Table 1 indicate that epoxy-group adsorption results in GO structures with stronger cohesion than hydroxyl-group adsorption, both for 100% and 50% coverages. This is attributed to less deformation of, and hence less stress induced in, the carbon hexagonal lattice as an oxygen atom in an epoxy group connects to neighboring carbon atoms and therefore the level of buckling is less than that caused by adsorption of hydroxyl groups alternating on two sides of the graphene lattice. Comparing 100% and 50% cases for each type of coverage (either epoxy or hydroxyl group), one notices that 100% coverages have smaller absolute cohesive energies than corresponding 50% coverages. This can also be explained by less deformation of the carbon hexagonal lattice in the 50% cases as compared to 100% cases. For comparison, we obtain cohesive energy of pristine graphene to be -9.577 eV/atom comparable to available values from the literature calculated for graphite and graphene using different methods [52-56]. Therefore, the change of cohesive energy shows a trend of reduction in its absolute value upon increasing surface coverage from 0% (pure graphene) to 50% to 100%, for both epoxy- and hydroxyl-group coverages. The hybrid structure 75-GO-GOH-OPT with 75% coverage has a cohesive energy with absolute value smaller than those for 50% one-type coverages (either epoxy or hydroxyl group). Although cohesive energy analysis does not directly relate to GO exfoliation, nevertheless it contains useful information on the relative stability of GO with different coverages.

In order to interpret van der Waals energy results presented in Table 1, we consider the relaxed structures shown in Figs. 1 and 2. From Fig. 1 it is clear that 100-GO-OPT structure corresponds

to a compact arrangement where the negatively charged oxygen atoms from one layer face the positively charged carbon atoms from the other layer. This compact arrangement results in largest absolute van der Waals interaction energy. Upon relaxation, the 50-GO-OPT structure nearly assumes an AA configuration that mimics the compact arrangement of relaxed 100-GO-OPT structure. However, as 50-GO-OPT has 50% less epoxy groups, the layers get closer to each other but the number of charged regions from adjacent layers is smaller compared to the 100-GO-OPT case resulting in weaker interlayer van der Waals interactions. Comparing 100-GOH-OPT and 50-GOH-OPT cases whose optimized structures are depicted in Fig. 1, Table 1 shows that despite larger number of hydroxyl groups the former structure has less absolute van der Waals interaction energy than the latter owing to smaller interlayer separation in the 50% coverage case. For the 75-GO-GOH-OPT structure we obtain the interlayer energy between the cases of pure epoxy- and hydroxyl-group coverages, owing to the competing nature of the aforementioned effects in the hybrid case.

It should be mentioned that the average interlayer distances for minimum-energy bilayer square platelets obtained from UFF calculations (presented in Table 1) are generally smaller than the interlayer distance equal to 6.3 Å reported in the literature for dry GO [57]. Only the interlayer distance for the 100-GOH-OPT structure (6.27 Å) agrees with the experimental value. A possible explanation is that arrangement of oxygen-containing groups in experiments is random, and therefore for strong oxidation the hydroxyl groups prevent the layers from getting closer than the aforementioned distance.

Effective force constants $k_{sh,i}$ for shifts and $k_{t,i}$ for tilts, calculated according to the procedure explained in Section 2 upon small shift/tilt around minimum energy configurations of bilayer GO, are presented in Table S1 of the ESI.

3.2. Adsorption of water molecules

In order to calculate energetics of water adsorption on GO, we consider adsorption of a single layer of water molecules on one side of single layer GO structures with 100%, 50%, and 75% coverages. Unit cells including eight carbon atoms are used to calculate adsorption of one water molecule per single layer GO for the optimized structures depicted in Figs. 1 and 2, except for 100-GOH-OPT for which a two-carbon atom unit cell is used. Different initial guesses are assumed for the initial positions of the water molecule on GO structures, and the periodic structures are optimized within DFT-LDA. A vertical unit cell dimension of 26-32 Å, depending on structure, was chosen to avoid interaction with other GO layers. The resulting optimized structures are depicted in Fig. 3.

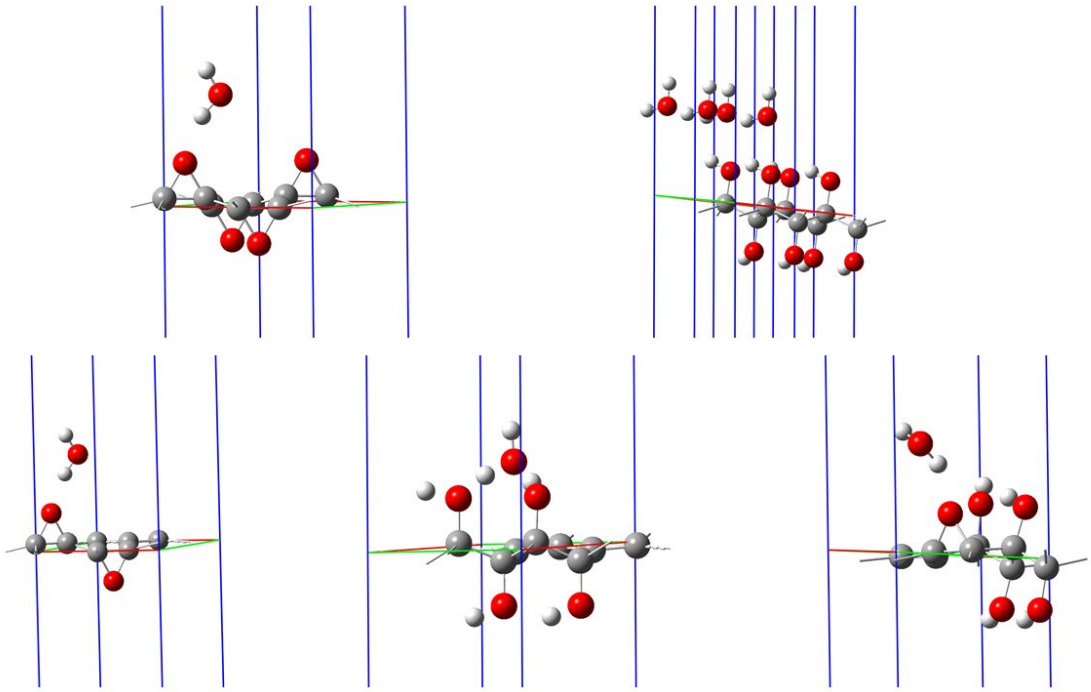

Figure 3: Graphene-oxide structures containing 8 carbon atoms with adsorbed water optimized within DFT-LDA.

Adsorption energies are calculated with respect to the state where the water molecule and each GO structure are separated, and the results are presented in Table 2. The adsorption energies are taken to be per molecule per adsorption site, i.e. either epoxy or hydroxyl group. It is noticed that for high coverage density, interactions among water molecules arranged by the underlying GO lattice are stabilizing. Specifically, for 100-GOH-OPT structure with one water molecule adsorbed on one side of GO sheet per two carbon atoms, removing the underlying GO lattice and calculating energy of water molecules show that the arranged water layer is more stable by 0.836 eV/molecule than separated molecules (independent of supercell size). This is of course for very ordered and most tightly-packed water layer that can adsorb on GO. It should be mentioned that when coverage is less than 100%, adsorption of more than one water molecule per adsorption site may become possible. We discuss the implication of this possibility in Section 3.3. We define the average distance between water molecule and GO sheet as the average z-coordinate of water molecule minus the average z-coordinate of carbon atoms. These average distances are presented in Table 2, and will be used to calculate energetics of exfoliation in Sections 3.4, 3.5, and 3.5.

Table 2: Energetics of water adsorption on different GO structures.

Coverage	100%	100%	50%	50%	75%

Structure	100-GO-OPT	100-GOH-OPT	50-GO-OPT	50-GOH-OPT	75-GO-GOH-OPT
Oxygen-containing group	epoxy	hydroxyl	epoxy	hydroxyl	Mixture of epoxy and hydroxyl
Adsorption energy per water molecule per adsorption site (eV)	0.575	0.992	0.537	1.080	0.852
Average distance between water molecule and GO sheet (Å)	3.66	4.55	3.70	2.95	3.66

From the results in Table 2 we notice that largest adsorption energy corresponds to adsorption on hydroxyl groups while the smallest adsorption energy corresponds to adsorption on epoxy groups. The reason is that epoxy groups provide only oxygen sites for hydrogen bonding with water molecules, whereas hydroxyl groups provide both oxygen and hydrogen sites. The energy for water adsorption on mixed epoxy-hydroxyl groups is between the two cases for pure epoxy and hydroxyl groups.

3.3. Parallel exfoliation and prevention of restacking by water adsorption

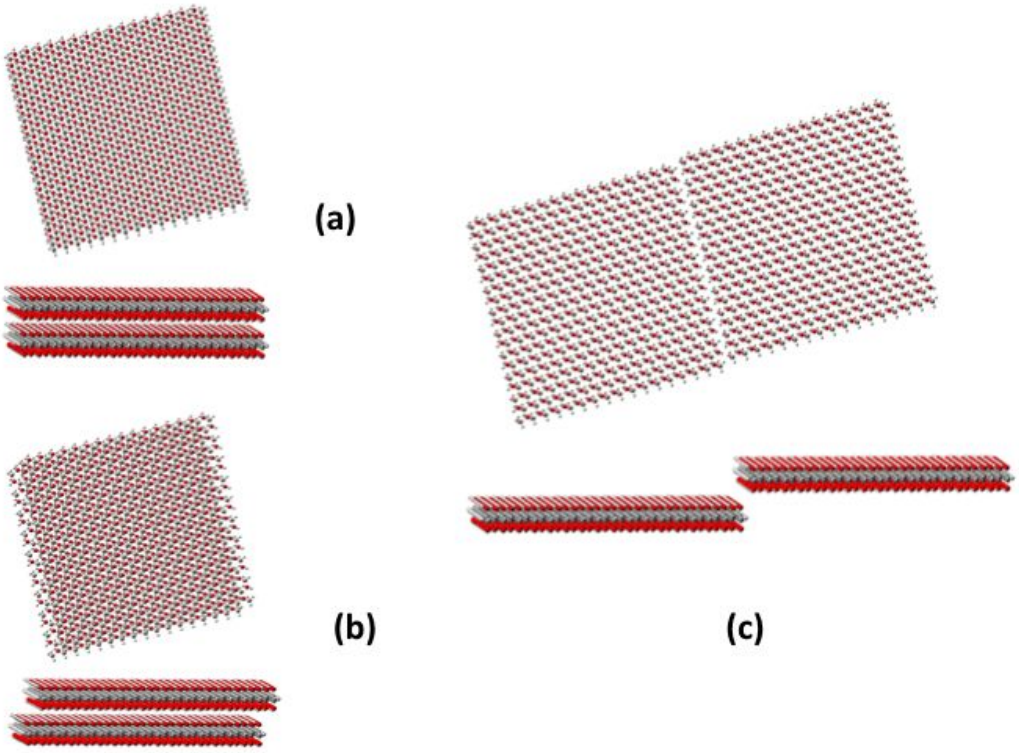

Figure 4: Schematic top (perpendicular to the 2D sheets) and side (parallel to the 2D sheets) views of three stages of parallel exfoliation, i.e., exfoliation with fixed interlayer distance, of graphene oxide square nanoplatelets with 40 Å sides: Stacked configuration (a), one step of parallel exfoliation (b), and verge of complete exfoliation (c). Water molecules (not shown) provide a locking mechanism that prevents restacking after (partial) exfoliation.

Different stages of parallel exfoliation are depicted in Fig. 4 for graphene oxide square nanoplatelets with 40 Å sides. The square nanoplatelets are used to calculate the changes in interlayer energy ΔU_{int}, and the partition functions needed to obtain changes in entropy and free energy ΔG [(Eq. (6)] at the verge of exfoliation. The results are presented in Table 3.

Table 3: Overall changes in internal potential energy ΔU_{int}, kinetic contribution $k_{\mathrm{B}}T\ln\left(q_{exf}/q_{sta}\right)$, and free energy ΔG between verge of parallel exfoliation and stacked states [Fig. 4(a) and (c)] for the bilayer square 40 Å nanplatelets based on the optimized structures depicted in Figs. 1 and 2. The interlayer distances are set at their UFF equilibrium values and temperature is 298 K. Bold values in parentheses correspond to one step of parallel exfoliation [Fig. 4(b)].

Structure	100-GO-OPT	100-GOH-OPT	50-GO-OPT	50-GOH-OPT	75-GO-GOH-OPT
ΔU_{int} (eV)	41.089 **(0.950)**	38.676 **(0.853)**	34.607 **(3.935)**	37.757 **(1.610)**	32.950 **(1.329)**
$\frac{\Delta U_{int}}{\varepsilon}$ (eV)	0.525 **(0.012)**	0.494 **(0.011)**	0.442 **(0.050)**	0.482 **(0.021)**	0.421 **(0.017)**
$k_{\mathrm{B}}T\ln\left(\frac{q_{exf}}{q_{sta}}\right)$ (eV)	0.437	0.430	0.413	0.452	0.374
ΔE_{ads} (eV)	94.875 **(2.875)**	327.360 **(9.920)**	47.437 **(1.437)**	163.680 **(4.960)**	175.725 **(5.325)**
$\gamma\Delta A$ (eV)	7.181 **(0.460)**	7.181 **(0.463)**	7.181 **(0.460)**	7.181 **(0.463)**	7.181 **(0.461)**
ΔG (eV)	-175.082 **(-4.818)**	-640.079 **(-18.903)**	-74.007 **(-1.716)**	-341.782 **(-9.853)**	-336.854 **(-9.711)**

We notice that parallel exfoliation happens in steps, first of which corresponds to exposing, e.g., one row of water adsorption sites. (Depending on nanoplatelets' geometry, such first step can correspond to exposing only a single adsorption site. This will be discussed below.) Therefore, in addition to overall changes between the verge of exfoliation and stacked states, Table 3 also includes (as bold values) changes between one step of parallel exfoliation and stacked states, schematically shown in Figs. 4(b) and (a), respectively. Bold values are not shown for the kinetic contribution $k_{\mathrm{B}}T\ln\left(q_{exf}/q_{sta}\right)$ as it is considered to be small in comparison. As there are different routes to parallel exfoliation, the bold values in Table 3 correspond to the "easiest" first steps with smallest increase in interlayer energy upon exposing one row of water adsorption sites. It is noted that the overall changes in free energy are all negative, both at verge of exfoliation and after one step. Water adsorption energy is found to be large enough to overcome the energy increase caused by new solvent surface generation and interlayer energy rise. This exothermic nature of the overall process is dictated by the dominant values of the adsorption energy ΔE_{ads}, that can "lock" the partially exfoliated system, prevent restacking, and allow only further exfoliation steps to happen.

From Table 3 we notice that, at temperatures of practical interest, the main contributions to free energy change come from the adsorption energy ΔE_{ads} and solvent surface generation energy $\gamma\Delta A$. The change in screened interlayer energy $\Delta U_{int}/\varepsilon$ and the kinetic contribution $k_{\mathrm{B}}T\ln\left(q_{exf}/q_{sta}\right)$ are much smaller in comparison. It is worth mentioning that the change in internal potential energy upon exfoliation ΔU_{int} can be compared with a typical GO surface energy value of 62.1 mJ/m^2 [58]: For the case of 75-GO-GOH-OPT, e.g., ΔU_{int} is equal to 329 mJ/m^2. The difference can be attributed to the specific surface coverage (type and amount) that can be different from those in

experiments. This is in line with the difference between our calculated interlayer distances and the experimental one mentioned in sections 3.1.

ΔE_{ads} for all structures are calculated assuming one water molecule per adsorption site. As mentioned in Section 3.2, coverages lower than 100% may allow more than one water molecule to adsorb per adsorption site. Adsorption energy per site for such lower coverages may seem to be larger than those presented in Table 3. However adsorption of more than one water molecule per adsorption site (epoxy and hydroxyl) means less stabilizing interaction among adsorbed water molecules, as well as less adsorption energy per water molecule because of sterical hindrance. Owing to these competing effects, ΔE_{ads} values based on one water molecule per adsorption site are assumed to be approximately valid for coverages lower than 100%.

It should be noticed that *before* water adsorption can happen, the process should overcome an energy increase at least equal to the sum of $\Delta U_{int}/\varepsilon$ and $2\gamma\Delta A$. For a possible actual process, this increase can be minimized by exposure of minimum surface area that exposes a minimum number (possibly one) of water adsorption sites. In addition, it is necessary for the platelets to overcome the energy increase associated with the interlayer van der Waals interactions readjustment during parallel movement that is the shift or rotation necessary to expose water adsorption site(s). A previous estimate [59] determined such energy increase to have a maximum value of 1.1 meV/atom corresponding to Lennard-Jones modeling of van der Waals interlayer interactions for graphene. This contribution can be larger for GO compared to graphene. Assuming that the corresponding energy rise per atom is only moderately larger than that for graphene, for the whole

GO bilayer with 40 Å side lengths and 660 carbon atoms per layer, this contribution is estimated to be about the same order as ΔU_{int} for one step of parallel exfoliation. It should be noticed that this contribution reduces as the overlapping areas of the two layers reduce during parallel exfoliation. The surface-area-dependent readjustment of interlayer van der Waals interactions during parallel movement are further discussed in section 3.6 below.

3.4. Perpendicular exfoliation upon water intercalation

In this section we consider the exfoliation route perpendicular to the nanoplatelet's surface. The calculated adsorption energies for a single layer of water molecules on GO nanoplatelets are provided in Table 2. For intercalation of one-molecule-thick layer of water between the two layers of a GO bilayer structure, the adsorption energy ΔE_{ads} is estimated to be twice these values, assuming almost same binding energies between each water molecule and each of the two layers. The internal energy increase ΔU_{int} in each case is calculated for bilayer square sheets, with 40 Å side length, at increased interlayer distance owing to water intercalation. These distances are estimated assuming that both GO nanoplatelets have the same distance from the (middle of) single layer of intercalated water molecules based on the DFT-LDA relaxation results. Intercalation of a single layer of water molecules is the first step in perpendicular exfoliation. Intercalation of a second layer of water molecules results in the system at the verge of full perpendicular exfoliation. Interlayer distances at this stage are obtained by adding average inter-molecular distance of water that is 2.82 Å [60] to the values for the first step. The characteristics of perpendicular exfoliation are presented in Table 4. We notice that the overall change of free energy is negative, and almost the same, for the first and the second steps of perpendicular exfoliation. Despite the fact that these

steps are exothermic overall, the corresponding processes should overcome an energy increase equal to the sum of ΔU_{int} and $2\gamma\Delta A$ *before* water intercalation and reduction of energy due to adsorption can happen.

Table 4: Characteristics for perpendicular exfoliation upon intercalation of two layers of water molecules. Bold values in parentheses correspond to one step of perpendicular exfoliation (intercalation of one layer of water molecules). Notice that ΔE_{ads} for intercalation of one and two layers of water molecules corresponds to the same adsorption configuration on exposed surfaces, and therefore are equal. The kinetic contributions $k_B T \ln\left(q_{exf}/q_{sta}\right)$ are taken to be the same as those in Table 3, and therefore are not included.

Structure	100-GO-OPT	100-GOH-OPT	50-GO-OPT	50-GOH-OPT	75-GO-GOH-OPT
Separation increase (Å)	5.69 **(2.87)**	5.65 **(2.83)**	5.92 **(3.10)**	3.39 **(0.57)**	4.35 **(1.53)**
ΔU_{int} (eV)	40.697 **(35.775)**	37.924 **(33.190)**	34.194 **(30.662)**	34.127 **(8.657)**	32.643 **(27.580)**
$\frac{\Delta U_{int}}{\varepsilon}$ (eV)	0.520 **(0.457)**	0.484 **(0.424)**	0.437 **(0.392)**	0.436 **(0.111)**	0.417 **(0.352)**
ΔE_{ads} (eV)	94.875 **(94.875)**	327.360 **(327.360)**	44.303 **(44.303)**	178.200 **(178.200)**	175.725 **(175.725)**
$\gamma\Delta A$ (eV)	7.181 **(7.181)**	7.181 **(7.181)**	7.181 **(7.181)**	7.181 **(7.181)**	7.181 **(7.181)**

ΔG (eV)	-175.087 **(-174.931)**	-640.089 **(-639.934)**	-74.014 **(-73.852)**	-341.828 **(-341.927)**	-336.858 **(-336.736)**

3.5. Exfoliation initiated by edge bending and water intercalation

The third possible exfoliation scenario that should be considered is intercalation of water molecules at the edge of the bilayer structures upon bending of one layer. In a system that contains a multi-layer structure instead of a bilayer one, the bent layer corresponds to one of the two outmost layers of the structure. In this section, we refer to this layer as the "top" layer. For calculating energy changes corresponding to water intercalation through edge bending, two contributions should be calculated: (1) intra-layer energy change as a result of bending the top layer, considered separate from the rest of the structure and (2) interlayer energy changes corresponding to (location-dependent) increase in inter-layer distances. Below, we explain each of these contributions separately.

In order to calculate intra-layer bending energy of a separate single layer, we perform ab initio calculations on parts of GO layers with 50%, 75%, and 100% epoxy and hydroxyl coverages. Parts in the form of nanoribbons with both armchair and zigzag edges are cut from the GO square sheets. Two structures with 50% coverage and armchair edge are depicted in Figs. 5 and 6 for epoxy and hydroxyl coverages, respectively. Two structures with 50% coverage and zigzag edge are depicted in Figs S2 and S3 of the ESI, for epoxy and hydroxyl coverages, respectively.

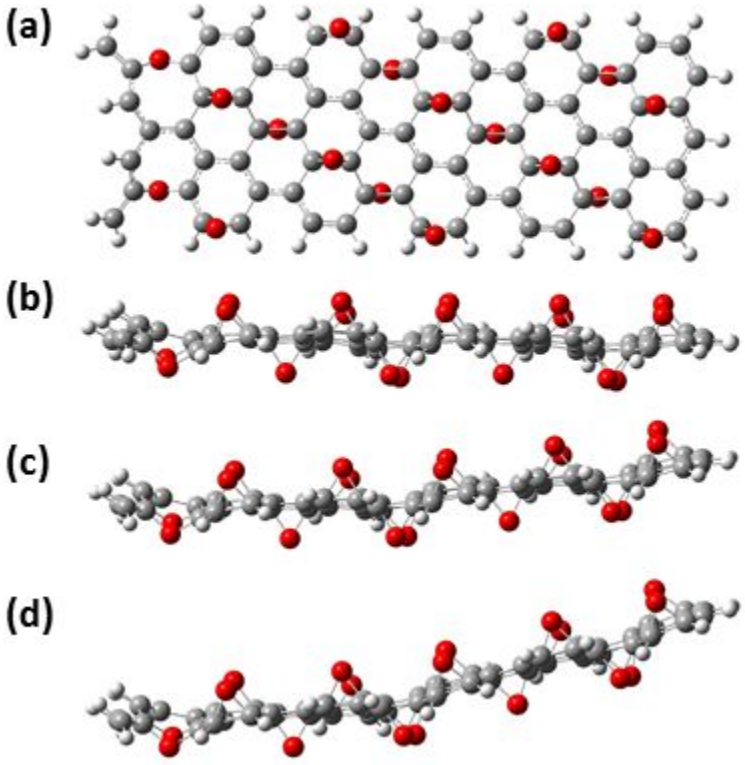

Figure 5: Top (a) and side (b) views of optimized GO nanoribbon with armchair edge and 50% epoxy coverage, as well as side views of its constrained optimization results with bent right edge to accommodate one (c) and two (d) water molecules.

To make the ab initio calculations manageable, the nanoribbon lengths are chosen to be almost half of the side length of GO square sheets (40 Å). Therefore, the heights to which the right edges of the nanoribbons should be raised to accommodate water molecules are half of the separation increases presented in Table 4. Constrained optimizations, within the ab initio framework explained in Section 2, are performed on bent structures while keeping two rows of carbon atoms at the left and right edges fixed. As such, the smooth curvature of the bent structure is determined by (constrained) ab initio optimization.

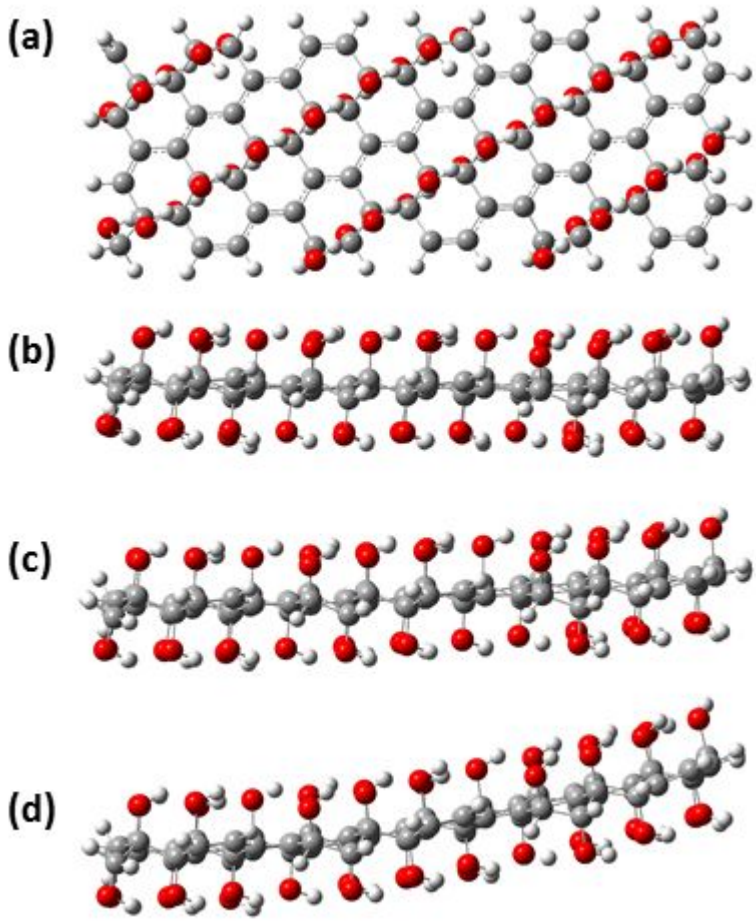

Figure 6: Top (a) and side (b) views of optimized GO nanoribbon with armchair edge and 50% hydroxyl coverage, as well as side views of its constrained optimization results with bent right edge to accommodate one (c) and two (d) water molecules.

The initial bent nanoribbon structures are prepared by bending the flat optimized structures at their middle, keeping the two sides straight, such that the right edge is raised to the desired height. Constrained optimization results in a smooth curvature instead of the initial abrupt bent at the middle. There can be a length difference between the initial abruptly bent and optimized structures (Fig. S4 of the ESI). Considering the base planes of GO nanoribbons as the neutral surface [61],

i.e. with no length change upon optimization after bending compared to the length of optimized flat structure, we adjust the length while preparing the initial structures before optimization. This ensures that unrealistic stress is not introduced in the bent structure to affect energetics. The nanoribbon intra-layer energy changes are shown in Table S2 of the ESI. It is observed that some of the energy changes are negative, i.e., the optimized bent structure has lower energy than that of the corresponding optimized flat structure. This is because of the interactions among the surface functional groups (epoxy and hydroxyl), and can happen only upon passing an energy barrier. Calculation of the barrier is computationally demanding and not performed here. We therefore focus on the energies of final optimized structures, and exclude the negative energy changes from further consideration. The intra-layer energy changes for the square plates with 40 Å sides are obtained by averaging the positive results for the nanoribbons with the same functional group and different edge geometries (armchair and zigzag), and multiplying the average by the ratio of the areas of the square nanoplate and the nanoribbon.

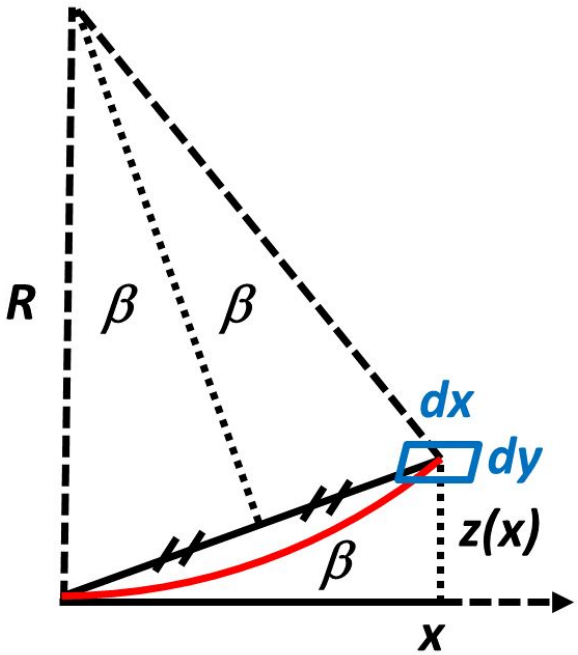

Figure 7: Schematics of the continuum model used to estimate the inter-layer energy change upon bending.

We use a continuum model based on Lennard-Jones (L-J) potential to determine interlayer energy changes upon bending. The inter-layer energy changes corresponding to (location-dependent) increase in inter-layer distances are calculated as

$$\Delta U_{inter} = \left\{ \frac{1}{X_0 Y_0} \int_0^{Y_0} \int_0^{X_0} 4\varepsilon_{L-J} \left[\left(\frac{\sigma}{z} \right)^{12} - \left(\frac{\sigma}{z} \right)^{6} \right] dxdy \right\} + \varepsilon_{L-J}, \quad (7)$$

where X_0 and Y_0 are the lateral dimensions of the square nanoplatelet, ε_{L-J} and σ are the L-J parameters (the former being equal to the negative of minimum interlayer energy), and z is the height increase upon bending for the arbitrary surface element $dxdy$ compared to its equilibrium value (Fig. (7)). The L-J parameters σ and ε_{L-J} are determined by fitting interlayer equilibrium distance and interlayer energy rise upon adsorption of two layers of water molecules (given in Table 4), respectively. These parameters for different systems are given in Table S3 of the ESI. We consider that the nanoplatelet's edge at X_0 is uniformly raised to $z_{\max}$, and that $\beta = \tan^{-1}(z/x)$ is the angle representing the rise of an arbitrary surface element $dxdy$ depicted in Fig. 7. Equation (7) can then be written as

$$\Delta U_{inter} = \left\{ \frac{4\varepsilon_{L-J}}{X_0} \int_0^{X_0} \left[\left(\frac{\sigma}{z} \right)^{12} - \left(\frac{\sigma}{z} \right)^{6} \right] dx \right\} + \varepsilon_{L-J}, \quad (8)$$

in which $z = R(1 - \cos 2\beta)$, $x = R\sin 2\beta$, and the curvature radius R is given by

$$R = \frac{X_0^2 + z_{max}^2}{2z_{max}}. \quad (9)$$

Using these relations, the integral in Eq. (8) is calculated numerically. For calculating the free energy changes upon edge bending and water intercalation, Eq. (6) is modified as follows:

$$\Delta G = \Delta U_{int} - 0.5 k_B T \ln\left(\frac{q_{exf}}{q_{sta}}\right) + 2\gamma\Delta A - 2\Delta E_{ads}, \quad (10)$$

in which $\Delta U_{int} = \Delta U_{intra} + \Delta U_{inter}$. The reason for not dividing the internal energy by the dielectric constant of water is that ΔU_{intra} is not screened by water and screening of ΔU_{inter} by water intercalation only at the edge is insignificant: Intercalation of water just at the bent edge covers a negligible area compared to the whole bent surface of the top layer. (Further intercalation and adsorption of water at inner sites results in step-by-step screening of the interlayer interactions corresponding to the surfaces covered by water, in accordance to Eq. 6). Energetics of exfoliation via edge bending are presented in Table 5.

Table 5: Energy characteristics for bending to accommodate two water molecules intercalation at the edge. Bold values in parentheses correspond to one water molecule intercalation at the edge. The kinetic contributions $k_B T \ln(q_{exf}/q_{sta})$ are taken to be negligible for these first two stages of edge exfoliation and therefore are not included.

Structure	100-GO-OPT	100-GOH-OPT	50-GO-OPT	50-GOH-OPT	75-GO-GOH-OPT
ΔU_{intra} (eV)	-	0.968	0.512	0.376	1.024

	(5.104)	**(0.520)**	**(0.320)**	**(0.080)**	**(0.368)**
ΔU_{inter} (eV)	22.588 **(15.856)**	18.498 **(11.634)**	19.531 **(14.356)**	14.521 **(1.906)**	14.848 **(6.058)**
ΔU_{int} (eV)	- **(20.960)**	19.466 **(12.154)**	20.043 **(14.676)**	14.897 **(1.986)**	15.872 **(6.426)**
ΔE_{ads} (eV)	2.875 **(2.875)**	9.920 **(9.920)**	1.437 **(1.437)**	4.960 **(4.960)**	5.325 **(5.325)**
$\gamma \Delta A$ (eV)	0.460 **(0.460)**	0.463 **(0.463)**	0.460 **(0.460)**	0.463 **(0.463)**	0.461 **(0.461)**
ΔG (eV)	- **(16.130)**	0.552 **(-6.760)**	18.089 **(12.722)**	5.903 **(-7.008)**	6.144 **(-3.302)**

It should be noticed that the non-bold contents of Table 5 are different from the corresponding contents of Tables 3 and 4, as Table 5 does not include energetics of the systems at the verge of full exfoliation. The bold values in Table 5 represent energies for bending and accommodating one water molecule at each of the exposed adsorption site pairs at the edge. Non-bold values in Table 5 represent energies for bending and accommodating two water molecules at each of the exposed adsorption site pairs at the edge (one water molecule per layer). This latter configuration does not represent the system at the verge of exfoliation, nevertheless, it represents a configuration through which further intercalation of water molecules can occur beyond just the adsorption sites at the edge. Further water intercalation increases the bending degree of the top layer to accommodate adsorption of water molecules at inner sites.

Based on exclusion of negative intra-layer energy changes as discussed above, the energetics the the 100-GO-OPT structure with two-water-molecule intercalation at the edge is indeterminate in our calculations. Nevertheless, the rest of the contents in Table 5 can be used together with Tables 3 and 4 to draw general conclusions.

3.6. Comparison of different exfoliation scenarios

Consider the first step of exfoliation processes before water adsorption (and hence interlayer interaction screening) happens. According to Tables 3, 4, and 5, the contribution of the (unscreened) internal potential energy change (ΔU_{int}) is the dominant contribution to increase the free energy change. For the parallel exfoliation case, as explained before, the energy increases associated with the readjustment of van der Waals interactions during parallel movements of the two layers should also be included. An estimate based on maximum increase for graphene results in about the same energy increase as that owing to ΔU_{int}. For ease of comparison, we reproduce the ΔU_{int} results for the first step of different exfoliation mechanisms in Table 6. Comparing the ΔU_{int} contributions to free energy rise during the first steps of parallel, perpendicular, and edge exfoliations, we see that parallel exfoliation is the most feasible, perpendicular exfoliation is the least feasible, and edge exfoliation is between these two limits. Even if the contribution from the readjustment of van der Waals interactions during parallel movements is an order of magnitude larger for graphene oxide compared to that for graphene, parallel exfoliation is still more feasible than edge exfoliation (that itself is more feasible that perpendicular exfoliation).

Table 6: Unscreened ΔU_{int} contributions to free energy rise for the first step of parallel (*par*), perpendicular (*per*), and edge exfoliations (*edg*), reproduced from Tables 3, 4, and 5, respectively.

Structure	100-GO-OPT	100-GOH-OPT	50-GO-OPT	50-GOH-OPT	75-GO-GOH-OPT
$\Delta U_{int,par}$ (eV)	**0.950**	**0.853**	**3.935**	**1.610**	**1.329**
$\Delta U_{int,per}$ (eV)	**35.775**	**33.190**	**30.662**	**8.657**	**27.580**
$\Delta U_{int,edg}$ (eV)	**20.960**	**12.154**	**14.676**	**1.986**	**6.426**

The main reason behind the aforementioned feasibility assessment is the level of interlayer distance increase during different exfoliation scenarios: While perpendicular and edge exfoliations involve full and partial systematic increase of interlayer distance, this increase is basically negligible for parallel exfoliation. Here we assume that, despite the presence of functional group (epoxy and hydroxyl), it is still possible for the two layers to slide parallel to one another (including possible relative rotations) without significant interlayer distance increase. This generally applies to low surface coverages or high surface coverages, provided that the contribution from the readjustment of van der Waals interactions is only moderately larger than that for graphene. If the coverage is neither low nor high, e.g. for random 50% coverage, one layer's functional groups can face areas from the other layer that do not have functional groups with a high density. "Parallel" exfoliation in this case may involve partial climbs and/or significant contribution from the readjustment of van der Waals interactions. In such cases, edge exfoliation can become more

feasible than the "parallel" one. As was mentioned in section 3.1, however, our calculated interlayer distances are generally smaller than the reported experimental value. This can indicate possibility of parallel movement under experimental conditions.

Another issue that needs to be mentioned is as follows: For edge exfoliation that the intra-layer energy increases are much smaller than the interlayer energy increases, why should the systems have smooth curvatures along the whole length of the platelets? Is it not more energetically favorable for the systems to bend abruptly to accommodate water molecules at the edge, and keep the optimal interlayer distance for the rest of the platelets? The answer depends on the system size and coverage. For the particular system size and coverages that we include here, abrupt bending is not feasible as it results in smaller radii of curvature than those considered and result in some negative intra-layer energy changes (Table S2 of the ESI). These indicate that the system should overcome an energy barrier to reach a configuration with attractive interactions among the functional groups. For yet smaller radii of curvature, these intra-layer energy barriers will be more significant. A comprehensive study of the size and coverage effects on the edge bending geometry is beyond the scope of the current work.

As we explained in the previous sections, the interactions between the GO plates crucially depend on their surface coverage and size. These affect both exfoliation and aggregation mechanisms. A study on the aggregation kinetics of GO plates [62] found that degree of aggregation in dispersed GO solutions depended on the ion concentration in and pH of the solution. The size (square root of the area) distribution was 200-900 nm, with a peak at 500 nm, that is much larger than the size of GO plates in our study (4 nm). The observed increase of aggregation upon ion-concentration

increase or pH decease was attributed to the cross-linking and interlayer interaction decrease in particular at the edge. Owing to the lack of specific information on surface coverage ratio in experiments, as well as size difference and absence of extra ions in our calculations, a direct quantitative comparison with our results cannot be made. However, the highlighted competing effects of hydrophilic interactions at functional groups and hydrophobic interactions at bare areas of the GO surface qualitatively agree with our results. Furthermore, it has been shown that increased ionic concentration in water results in decreased dielectric constant [63,64]. It can be seen from Eq. 6 that decreased dielectric constant results in increased free energy change, and hence less feasible exfoliation. This is consistent with increased restacking observed in Ref. [62] upon increased ionic concentration.

As mentioned before, the methodology for assessing thermodynamic energetics of liquid-phase exfoliation explained here is general and applicable to other 2D nanomaterials beyond GO. For pristine nanomaterials such as graphene, black phosphorus, and molybdenum disulfide, with hydrophobic tendency of surface interactions, adsorption energy should be calculated for the type and concentration of surfactants that are included to assist exfoliation. As for solvents other than water, using their surface energy and dielectric constant in Eqs. (6) and (10) would modify the calculations accordingly. The measurable characteristics that indicate efficiency of exfoliation such as yield of monolayers and stability of the dispersion depend on the dominant exfoliation mechanism as well as its kinetics. While we estimate overall energetics of different mechanisms, we do not consider exfoliation kinetics ibn this study. Our results are therefore useful for comparing energetics of different mechanisms, and the effects of the surface coverage (of functional groups and/or surfactants) as well as the size of the nanoplates.

4. Conclusions

In conclusion, using multi-scale computational modeling, we assess the feasibility of different routes to graphene oxide (GO) liquid-phase exfoliation for various GO coverages. Internal energy, entropy, and free energy changes are calculated for various oxidation percentages and functional groups (epoxy, hydroxyl, and their mixture). It is shown that the kinetic contribution to free energy change is small compared to other contributions. For the GO platelet size and coverages considered here, quantitative estimates of free energy changes indicate the feasibility of step-by-step parallel exfoliation via water adsorption that prevents restacking, compared to edge and perpendicular exfoliation scenarios. This is explained by comparing different contributions to free energy changes, in particular intra-layer and unscreened interlayer energy changes. The methodology can be used to calculate and compare energetics of different exfoliation routes for 2D systems with various sizes and coverages.

Acknowledgments

This research was supported by the National Science Foundation STTR Phase II grant IIP-1057999. The authors thank V. I. Pupyshev for very fruitful discussions.

References

[1]

Y. Hernandez, V. Nicolosi, M. Lotya, F. M. Blighe, Z. Sun, S. De, I. T. McGovern, B. Holland, M. Byrne, Y. K. Gunko, J. J. Boland, P. Niraj, G. Duesberg, S. Krishnamurthy, R. Goodhue, J. Hutchison, V. Scardaci, A. C. Ferrari, J. N. Coleman,

Nature Nanotechnology, 2008, **3**, 563−568.

[2]

A. B. Bourlinos, V. Georgakilas, R. Zboril, T. A. Steriotis, A. K. Stubos,

Small, 2009, **5**, 1841–1845.

[3]

J. N. Coleman,

Adv. Funct. Mater., 2009, **19**, 3680–3695.

[4]

K. Liu, L. Liu, Y. Luo, D. Jia,

J. Mater. Chem., 2012, **22**, 20342–20352.

[5]

G. S. Bang, K. W. Nam, J. Y. Kim, J. Shin, J. W. Choi, S.-Y. Choi,

ACS Appl. Mater. Interfaces, 2014, **6**, 7084−7089.

[6]

P. Yasaei , B. Kumar, T. Foroozan, C. Wang, M. Asadi, D. Tuschel, J. E. Indacochea, R. F. Klie, A. Salehi-Khojin,

Adv. Mater., 2015, **27**, 1887–1892.

[7]

H. He, J. Klinowski, M. Forster, A. Lerf,

Chem. Phys. Lett., 1998, **287**, 53−56.

[8]

T. Szabo, O. Berkesi, P. Forgo, K. Josepovits, Y. Sanakis, D. Petridis, I. Dekany,

Chem. Mater., 2006, **18**, 2740−2749.

[9]

H. C. Schniepp, J.-L. Li, M. J. McAllister, H. Sai, M. Herrera-Alonso; D. H. Adamson, R. K. Prud'homme, R. Car, D. A. Saville, I. A. Aksay,

J. Phys. Chem. B, 2006, **110**, 8535−8539.

[10]

A. Kaniyoor, T. T. Baby, S. Ramaprabhu,

J. Mater. Chem., 2010, **20**, 8467–8469.

[11]

M. Cardinali, L. Valentini, P. Fabbri, J. M. Kenny,

Chem. Phys. Lett., 2011, **508**, 285–288.

[12]

H.-B. Zhang, J.-W. Wang, Q. Yan, W.-G. Zheng, C. Chenb, Z.-Z. Yu,

J. Mater. Chem., 2011, **21**, 5392–5397.

[13]

V. Eswaraiah, S. S. J. Aravind, S. Ramaprabhu,

J. Mater. Chem., 2011, **21**, 6800–6803.

[14]

H. L. Poh, P. Simek, Z. Sofer, M. Pumera

ACS Nano, 2013, **7**. 5262–5272.

[15]

C. Botas, P. Alvarez, C. Blanco, R. Santamaria, M. Granda, M. D. Gutierrez, F. Rodriguez-Reinoso, R. Menendez,

Carbon, 2013, **52**, 476–485.

[16]

D. A. Dikin, S. Stankovich, E. J. Zimney, R. D. Piner, G. H. B. Dommett, G. Evmenenko, S. B. T. Nguyen, R. S. Ruoff,

Nature, 2007, **448**, 457−460.

[17]

Z. Wei, D. E. Barlow, P. E. Sheehan,

Nano Lett., 2008, **10**, 3141−3145.

[18]

N. R. Wilson, P. A. Pandey, R. Beanland, R. J. Young, I. A. Kinloch, L. Gong, Z. Liu, K. Suenaga, J. P. Rourke, S. J. York, J. Sloan,

ACS Nano, 2009, **3**, 2547–2556.

[19]

E. Kymakis, K. Savva, M. M. Stylianakis, C. Fotakis, E. Stratakis,

Adv. Funct. Mater., 2013, **23**, 2742–2749.

[20]

D.-W. Wang, C. Sun, G. Zhou, F. Li, L. Wen, B. C. Donose, G. Q. Lu, H.-M. Cheng, I. R. Gentle,

J. Mater. Chem. A, 2013, **1**, 3607–3612.

[21]

M. R. Karim, K. Hatakeyama, T. Matsui, H. Takehira, T. Taniguchi, M. Koinuma, Y. Matsumoto, T. Akutagawa, T. Nakamura, S.-I. Noro, T. Yamada, H. Kitagawa, S. Hayami,

J. Am. Chem. Soc., 2013, **135**, 8097−8100.

[22]

S. Stankovich, R. D. Piner, S. B. T. Nguyen, R. S. Ruoff,

Carbon, 2006, **44,** 3342–3347.

[23]

P. K. Ang, S. Wang, Q. Bao, J. T. L. Thong, K. P. Loh,

ACS Nano, 2009, **3**, 3587–3594.

[24]

M. B. Avinash, K. S. Subrahmanyam, Y. Sundarayya, T. Govindaraju,

Nanoscale, 2010, **2**, 1762–1766.

[25]

Y. Zhu, M. D. Stoller, W. Cai, A. Velamakanni, R. D. Piner, D. Chen, R. S. Ruoff,

ACS Nano, 2010, **4**, 1227–1233.

[26]

G.-L. Chen, S.-M. Shau, T.-Y. Juang, R.-H. Lee, C.-P. Chen, S.-Y. Suen, R.-J. Jeng,

Langmuir, 2011, **27**, 14563–14569.

[27]

S.-M. Shau, T.-Y. Juang, H.-S. Lin, C.-L. Huang, C.-F. Hsieh, J.-Y. Wua, R.-J. Jeng,

Polym. Chem., 2012, **3**, 1249–1259.

[28]

L. Zhang, J. Liang, Y. Huang, Y. Ma, Y. Wang, Y.Chen,

Carbon, 2009, **47**, 3365–3380.

[29]

T.-Y. Zhang, D. Zhang,

Bull. Mater. Sci., 2011, **34**, 25–28.

[30]

L. Chen, Z. Xu, J. Li, Y. Li, M. Shan, C. Wang, Z. Wang, Q. Guo, L. Liu, G.Chen, X.Qian,

J. Mater. Chem., 2012, **22**, 13460−13463.

[31].

S. Mayavan, J.-B. Sim, S.-M. Choi,

J. Mater. Chem., 2012, **22**, 6953−6958.

[32]

O. V. Pupysheva, A. A. Farajian, C. R. Knick, A. Zhamu, B. Z. Jang,

J. Phys. Chem. C, 2010**, 114***,* 21083−21087.

[33]

B. Z. Jang, A. Zhamu,

J. Mater. Sci., 2008, **43**, 5092–5101.

[34]

D. Boschetto, L. Malard, C. H. Lui, K. F. Mak, Z. Li, H. Yan, T. F. Heinz,

Nano Lett., 2013, **13**, 4620−4623.

[35]

F. Tran, R. Laskowski, P. Blaha, K. Schwarz,

Phys. Rev. B, 2007, **75**, 115131

[36]

B. Sahu, H. Min, A. H. MacDonald, S. K. Banerjee,

Phys. Rev. B, 2008, **78**, 045404.

[37]

P. Ordejón, E. Artacho, J. Soler,

Phys. Rev. B, 1996, **53**, R10441−R10444.

[38]

J. M. Soler, E. Artacho, J. D. Gale, A. García, J. Junquera, P. Ordejón, D. Sanchez-Portal,

J. Phys.: Condens. Matter, 2002, **14**, 2745−2779.

[39]

T. H. Osborn, A. A. Farajian, O. V. Pupysheva, R. S. Aga, L. C. Lew Yan Voon,

Chem. Phys. Lett., 2011, **511**, 101–105.

[40]

A. K. Rappe´, C. J. Casewit, K. S. Colwell, W. A. Goddard III, W. M. Skiff,

J. Am. Chem. Soc., 1992, **114**, 10024–10035.

[41]

M. J. Frisch, G. W. Trucks, H. B. Schlegel, G. E. Scuseria, M. A. Robb, J. R. Cheeseman, G. Scalmani, V. Barone, B. Mennucci, G. A. Petersson, H. Nakatsuji, M. Caricato, X. Li, H. P. Hratchian, A. F. Izmaylov, J. Bloino, G. Zheng, J. L. Sonnenberg, M. Hada, M. Ehara, K. Toyota, R. Fukuda, J. Hasegawa, M. Ishida, T. Nakajima, Y. Honda, O. Kitao, H. Nakai, T. Vreven, J. A. Montgomery Jr., J. E. Peralta, F. Ogliaro, M. Bearpark, J. J. Heyd, E. Brothers, K. N. Kudin, V. N. Staroverov, R. Kobayashi, J. Normand, K. Raghavachari, A. Rendell, J. C. Burant, S. S. Iyengar, J. Tomasi, M. Cossi, N. Rega, J. M. Millam, M. Klene, J. E. Knox, J. B. Cross, V. Bakken, C. Adamo, J. Jaramillo, R. Gomperts, R. E. Stratmann, O. Yazyev, A. J. Austin, R. Cammi, C. Pomelli, J. W. Ochterski, R. L. Martin, K. Morokuma, V. G. Zakrzewski, G. A. Voth, P. Salvador, J. J. Dannenberg, S. Dapprich, A. D. Daniels, O. Farkas, J. B. Foresman, J. V. Ortiz, J. Cioslowski, D. J. Fox,

Gaussian 09, revision A.02, Gaussian, Inc.: Wallingford, CT, 2009.

[42]

V. P. Carey,

Statistical Thermodynamics and Microscale Thermophysics.

Cambridge University Press, 1999, Section 4.2.

[43]

R. K. Pathria, P. D. Beale,

Statistical Mechanics, Third Edition.

Elsevier, 2011, Section 3.5.

[44]

Reference [36], Section 5.4.

[45]

D. H. Wertz,

J. Am. Chem. Soc., 1980, **102**, 5316−5322.

[46]

M. Mammen, E. I. Shakhnovich, J. M. Deutch, G. M. Whitesides,

J. Org. Chem., 1998, **63**, 3821−3830.

[47]

M. H. Abraham,

J. Am. Chem. Soc., 1981, **103**, 6742−6744.

[48]

J. Kua, J. E. Avila, C. G. Lee, W. D. Smith,

J. Phys. Chem. A, 2013, **117**, 12658−12667.

[49]

M. K. Rana, A. Chandra,

J. Chem. Phys., 2013, **138**, 204702.

[50]

G. Tocci, L. Joly, A. Michaelides,

Nano Lett., 2014, **14**, 6872−6877.

[51]

D. W. Boukhvalov, M. I. Katsnelson,

J. Am. Chem. Soc., 2008, **130**, 10697–10701.

[52]

J. Furthmüller, J. Hafner, G. Kresse,

Phys. Rev. B, 1994, **50**, 15606−15622.

[53]

B. I. Dunlap, J. C. Boettger,

J. Phys. B: At. Mol. Opt. Phys., 1996, **29**, 4907−4913.

[54]

L. Li, S. Reich, J. Robertson,

Phys. Rev. B, 2005, **72**, 184109.

[55]

N. Ooi, A. Rairkar, J. B. Adams,

Carbon, 2006, **44**, 231−242.

[56]

A. Quandt, C. Özdoğan, J. Kunstmann, H. Fehske,

Nanotechnology, 2008, **19**, 335707.

[57]

T. Szabó, A. Szeri, I. Dékány,

Carbon, 2005, **43**, 87−94.

[58]

Z. Lin, Y. Liu, C.-P. Wong,

Langmuir, 2010, **26**, 16110–16114.

[59]

I. V. Lebedeva, A. A. Knizhnik, A. M. Popov, O. V. Ershova, Y. E. Lozovik, B. V. Potapkin,

Phys. Rev. B, 2010, **82**, 155460.

[60]

A. V. Okhulkov, Y. N. Demianets, Y. E. Gorbaty,

J. Chem. Phys., 1994, **100**, 1578−1588.

[61]

L. D. Landau, E. M. Lifshitz,

Theory of Elasticity, 3rd Edition, Pergamon Press, Oxford 1986.

[62]

L. Wu, L. Liu, B. Gao, R. Muñoz-Carpena, M. Zhang, H. Chen, Z. Zhou, H. Wang,

Langmuir, 2013, **29,** 15174−15181.

[63]

J. B. Hasted, D. M. Ritson, C. H. Collie,

J. Chem. Phys., 1948, **16**, 1-21.

[64]

N. Gavish, K. Promislow,

Phys. Rev. E, 2016, **94**, 012611.